Materials Advances

ROYAL SOCIETY OF CHEMISTRY

PAPER

View Article Online
View Journal | View Issue

Cite this: *Mater. Adv.*, 2021, **2**, 366

Influence of La^{3+} induced defects on MnO_2–carbon nanotube hybrid electrodes for supercapacitors†

Nilanjan Chakrabarty,[ab] Monalisa Char,[a] Satheesh Krishnamurthy[c] and Amit K. Chakraborty*[ab]

Here, we report the successful coupling of La doped MnO_2 nanorods (30 nm mean diameter and 1 μm mean length) with multiwalled carbon nanotubes (CNTs) *via* a simple *in situ* hydrothermal method to form a La^{3+}:MnO_2–CNT nanohybrid as well as a systematic investigation of the influence of the dopant concentration on its performance as an electrode for supercapacitors. X-ray diffraction, electron microscopy and energy dispersive X-ray analysis revealed the formation of MnO_2 nanorods uniformly distributed within the CNT network. The electrochemical measurements revealed a strong positive influence of the La dopants on the performance of the MnO_2–CNT nanohybrid for up to 2 mol% La, above which the performance degraded. Thus, the 2 mol% La^{3+}:MnO_2–CNT nanohybrid sample was identified as the best electrode material in this study which exhibited a specific capacitance of ~1530 F g^{-1} at a current density of 1 A g^{-1} along with a charge retention of 92% after 5000 cycles which are both much higher than those reported previously for MnO_2 based supercapacitor electrodes and thus, is a leap towards using MnO_2 as a low-cost electrode for supercapacitors. The enhanced performance of the optimised 2 mol% La^{3+}:MnO_2–CNT nanohybrid originated from the combinatorial influence of the material selection, the optimised concentration of La dopants and the synergistic influence of CNTs that resulted in its lowest charge transfer resistance and highest diffusion coefficient.

Received 11th September 2020,
Accepted 14th November 2020

DOI: 10.1039/d0ma00696c

rsc.li/materials-advances

1. Introduction

As the demand for energy storage devices exhibiting a high power density rises, research on supercapacitors has received huge attention over the past couple of decades due to their high power output, fast charging or discharging and long cycle life.[1] The combination of these features makes the supercapacitor an effective component in modern electronic gadgets, electric vehicles, and industrial power set-ups. Of the two types of supercapacitors, electrical double layer capacitors (EDLCs) store energy on the electrode surface (typically using carbon nanomaterials such as CNTs, graphene, carbon aerogel, and activated carbon), whereas pseudocapacitors store energy by faradaic or redox reactions occurring at the electrode–electrolyte interface (typically uses transition metal compounds (TMCs) and conducting polymers).[2,3] Both EDLCs and pseudocapacitors have their own advantages and disadvantages. Manganese dioxide (MnO_2) is a TMC that has been widely investigated as a supercapacitor electrode owing to its high theoretical capacitance (1370 F g^{-1}), fast and reversible redox reaction, earth abundance, cost-effectiveness and eco-friendly nature;[4–7] however, its practical use has been limited due to poor electrical conductivity and poor capacity retention after a large number of cycles.

In order to overcome these demerits, some researchers have induced artificial defects into the MnO_2 lattice by introducing dopants (like Ag, V, B, Fe, Cu and Zn)[8–13] to improve the electrical conductivity of MnO_2, but the problem of poor cyclic stability still remains. Due to their good electrical conductivity, mechanical and chemical stability, and large specific surface area, CNTs have found widespread applications,[14–16] including in supercapacitors, as some researchers combined MnO_2 with multiwalled CNTs (MWCNTs) in order to improve both the electrical conductivity and cyclic stability of MnO_2.[17–23] These reports showed some improvements in the electrode performance as a result of doping of cations into MnO_2 and coupling

[a] *Carbon Nanotechnology Lab, Department of Physics, National Institute of Technology Durgapur, WB, 713209, India. E-mail: amit.chakraborty@phy.nitdgp.ac.in*
[b] *Centre of Excellence in Advanced Materials, National Institute of Technology Durgapur, WB, 713209, India*
[c] *Department of Engineering and Innovation, The Open University, Walton Hall, Milton Keynes, MK7 6AA, UK*

† Electronic supplementary information (ESI) available: Schematic of synthetic procedure, XPS spectra of C 1s, O 1s and La $3d_{3/2}$ of 2La–MnO_2–CNT, BET sorption and Ragone plot of undoped and 2 mol% La-doped MnO_2–CNT. See DOI: 10.1039/d0ma00696c

with CNTs but the value of specific capacitance still did not cross beyond a few hundred F g^{-1}. Interestingly, although a MnO_2 based electrode that is both doped with cations and coupled with CNTs is likely to have high performance due to synergistic influence on the electrical conductivity and cyclic stability, it has not been explored to date.

In view of the above, here we report a systematic investigation of the influence of La^{3+} dopants on the electrochemical performance of a MnO_2–CNT nanohybrid. A number of doped nanohybrid samples containing different concentrations of dopants were synthesized using a simple and low-cost hydrothermal method and the influence of dopants on their electrochemical performance was compared to identify the optimum dopant concentration.

2. Experimental

2.1 Materials required

CNTs were procured from NanoAmor Inc., USA. >98% pure manganese sulphate monohydrate ($MnSO_4{\cdot}H_2O$) purity), 99% pure (ammonium peroxydisulphate $(NH_4)_2S_2O_8$) (APS) and 97% pure sodium hydroxide pellets (NaOH) were procured from Merck, India. 99.9% pure lanthanum nitrate hexahydrate ($La(NO_3)_3{\cdot}6H_2O$) was procured from Alfa Aesar. Nafion pellets (NR-50) were procured from Sigma Aldrich. All chemicals were used as received from the supplier without any purification.

2.2 Synthesis of MnO_2–CNT and La^{3+}:MnO_2–CNT nanohybrids

First, for the synthesis of MnO_2–CNT nanohybrids, 25 mg of CNT was dissolved in 35 mL of double distilled water and ultrasonicated for 1 h. 0.1 M of $MnSO_4{\cdot}H_2O$ was then slowly introduced to the CNT suspension under constant stirring at 500 rpm. After 20 minutes, 35 mL of 0.1 M APS aqueous solution was then added to the $MnSO_4$–CNT suspension and stirred for another 1 h at 800 rpm. After stirring for a further 30 min, the resulting solution was transferred to a 100 mL Teflon lined stainless steel autoclave and kept at 140 °C for 24 h followed by a natural cooling step to room temperature. The reaction mixture was subsequently washed with deionised water until pH 7 and filtered, followed by a further wash with ethanol to remove any unreacted precursors (schematic in Fig. S1 of the ESI†). The final product was obtained as a powder of undoped MnO_2–CNT after drying the filtrate under an infrared lamp and named 0La–MnO_2–CNT.

To synthesize La^{3+}:MnO_2–CNT nanohybrids the same procedure was followed as above along with the addition of an appropriate amount of $La(NO_3)_3{\cdot}6H_2O$ to $MnSO_4{\cdot}H_2O$–CNT suspension. Several nanohybrid samples were prepared by varying the $La(NO_3)_3{\cdot}6H_2O$ content from 1, 2, 3 and 5 mol% with respect to $MnSO_4{\cdot}H_2O$ and named 1La–MnO_2–CNT, 2La–MnO_2–CNT, 3La–MnO_2–CNT and 5La–MnO_2–CNT, respectively.

2.3 Characterization techniques

PANALYTICAL X Pert Pro diffractometer was used to carry out the X-ray Diffraction (XRD) measurements for the powder samples and Cu Kα radiation (1.5414 Å) was employed as the X-ray source. Raman spectra were recorded using a Raman Spectrometer (LabRAM HR JobinYvon) with an argon ion laser (514.5 nm) and were calibrated with respect to the position of the Raman shift at 520 cm^{-1} originating from the Si wafer on which the sample was deposited.[16] Elemental mapping was carried out by using an Oxford Instruments energy-dispersive X-ray (EDX) analyser attached with a field emission scanning electron microscope (FESEM), (Carl Zeiss Supra 55, UK). A JEOL 2100 transmission electron microscope was used to collect the high resolution transmission electron microscope (HRTEM) images and the selected area electron diffraction (SAED) pattern and their analyses were performed using ImageJ software. XPS measurements were carried out at a base pressure of $\sim 6 \times 10^{-8}$ mbar using unmonochromated Mg Kα radiation giving an overall energy resolution of 1 eV. All spectra were calibrated by the position of the Au 4f peak originating from a gold foil in direct contact with the samples. The XPS peaks were fitted using CASA XPS software with a Shirley type background subtraction and Gaussian/Lorentzian peak shapes. The binding energies were corrected by setting the C 1s peak of adventitious carbon at 284.7 eV in accordance with those reported in the literature.[24,25] The specific surface areas of the samples were estimated from their N_2 adsorption isotherms at 77 K recorded using a BET surface analyzer (Nova 1000e, Quantachrome) after the samples were degassed at 300 °C for 3 h. The electrochemical testings were conducted with 1 M sodium hydroxide (NaOH) as the electrolyte in a 3-electrode cell comprising a glassy carbon disc (3 mm dia.) as the working electrode, Ag/AgCl as the reference electrode and Pt wire as the counter electrode using CHI 660E electrochemical workstation, USA. The working electrode was prepared by dropcasting a thick slurry of the active material (92%) and Nafion (8% as a binder) dissolved in a mixture of water and isopropanol in a 1 : 1 ratio (5 mg in 1 mL) on the glassy carbon disc followed by air drying. The estimation of diffusion co-efficient values and specific capacitance was carried out using standard methods reported in the literature.[26] The active material loading was 0.35 mg cm^{-2}.

3. Results and discussion

3.1 XRD analysis

The XRD pattern of the 0La–MnO_2–CNT sample presented in Fig. 1 shows peaks corresponding to the (110), (101), (011), (200), (112), (211), (220), (002) and (301) planes of the tetragonal phase of β-MnO_2 (*P*42/*mnm*, a = 4.39 Å, b = 4.39 Å and c = 2.87 Å) in accordance with JCPDS File no. 24-0735. A small peak at $2\theta = 26^\circ$ can be attributed to the (002) planes of CNTs in accordance with their small weight fraction. The crystallinity is significantly reduced in the XRD patterns for La^{3+} doped samples as evidenced from the presence of a few weak peaks corresponding to the orthogonal phase of α-MnO_2 (*Pnma*, a = 9.32 Å,

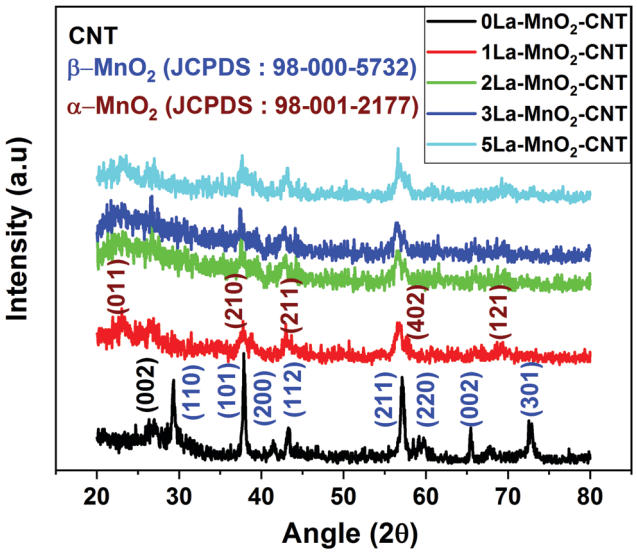

Fig. 1 XRD pattern of undoped and La^{3+}:MnO_2–CNT nanohybrid.

b = 2.85 Å and c = 4.46 Å) in accordance with JCPDS file no. 98-001-2177. The change in crystal structure from β-MnO_2 to α-MnO_2 and the transformation of polycrystalline β-MnO_2 to nearly amorphous α-MnO_2 could be due to the mismatch in the ionic radius of La and Mn which is in accordance with that previously reported in the literature.[9]

3.2 Raman analysis

The Raman spectra of the doped nanohybrids presented in Fig. 2(a) show an intense peak at 635 cm^{-1} corresponding to the symmetrical stretching mode of the Mn–O_8 vibrational unit, a Raman active mode for the tetragonal structure of β-MnO_2. An additional peak was observed at around 350 cm^{-1} for 3 mol% and 5 mol% La doping (inset of Fig. 2(a)) which can be attributed to the E_{2g} band of $La(OH)_3$.[27] Fig. 2(a) also shows two other intense and sharp peaks at 1580 cm^{-1}, and 1351 cm^{-1} due to the G and D bands of MWCNT, respectively.[28,29] The G band or graphitic band arises because of the in plane vibration of sp^2-bonded carbon atoms, whereas the D band arises because of structural defects such as change in bond angle and bond length that can break the symmetry. The ratio of the intensity of the D band (I_D) to that of G band (I_G) is often used as a measure of defects in carbonaceous systems like MWCNT[30,31] and hence these values are also shown in Fig. 2(b). It is evident that the value of I_D/I_G is increased from 0.75 for undoped sample to about 0.81 upon incorporation of 2 mol% La dopant. Interestingly, a further increase in dopant concentration did not cause significant change in this value. This can be understood by considering that at 2 mol% concentration, La^{3+} ions are able to cause sufficient defects on the MWCNT structure leading to the increase in the intensity of the D band. However, further increase in La concentration cannot cause any further damage to the MWCNTs, as these may form $La(OH)_3$.

3.3 Surface analysis

XPS was performed on the undoped and 2La–MnO_2–CNT nanohybrid samples to identify the surface chemical states of various elements within the nanohybrid samples. The Mn 2p XPS spectra of the undoped MnO_2–CNT and 2La–MnO_2–CNT samples are presented in Fig. 3(a and b), respectively, whereas the XPS spectra of all other elements are shown in Fig. S2 and S3 in the ESI.† It is evident from the deconvoluted spectra presented in Fig. 3 that both undoped and doped samples show the presence of a mixed Mn^{4+} and Mn^{3+} states in accordance with established literature reports.[32,33] In addition, for the 2La–MnO_2–CNT doped sample, the La 3d region showed a broad feature (due to the low weight fraction of La) corresponding to La^{3+} states[34] (Fig. S3c of the ESI†).

To assess the influence of dopants on the surface area of the MnO_2–CNT nanohybrid, BET sorption isotherms were measured for both the undoped and the 2La–MnO_2–CNT samples (Fig. S4 of the ESI†) which revealed a much larger value of 99 $m^2\ g^{-1}$ for the specific surface area of the 2La–MnO_2–CNT nanohybrid sample compared to that of the undoped MnO_2–CNT sample (63 $m^2\ g^{-1}$). The increased surface area of 2La–MnO_2–CNT clearly establishes the strong influence of the dopants on the

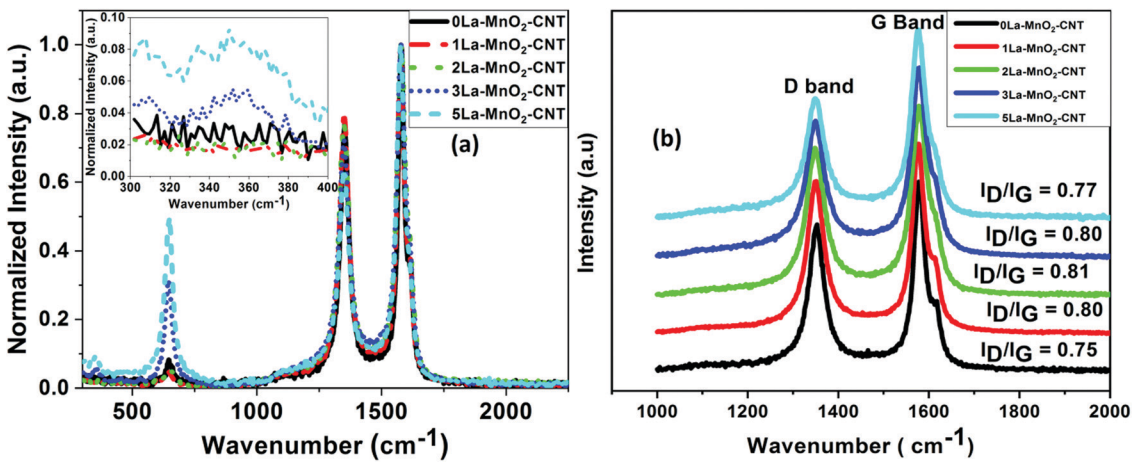

Fig. 2 Raman spectra of undoped and La-doped MnO_2–CNT (a); Raman spectra showing the D band and G band of undoped and La-doped MnO_2–CNT (b).

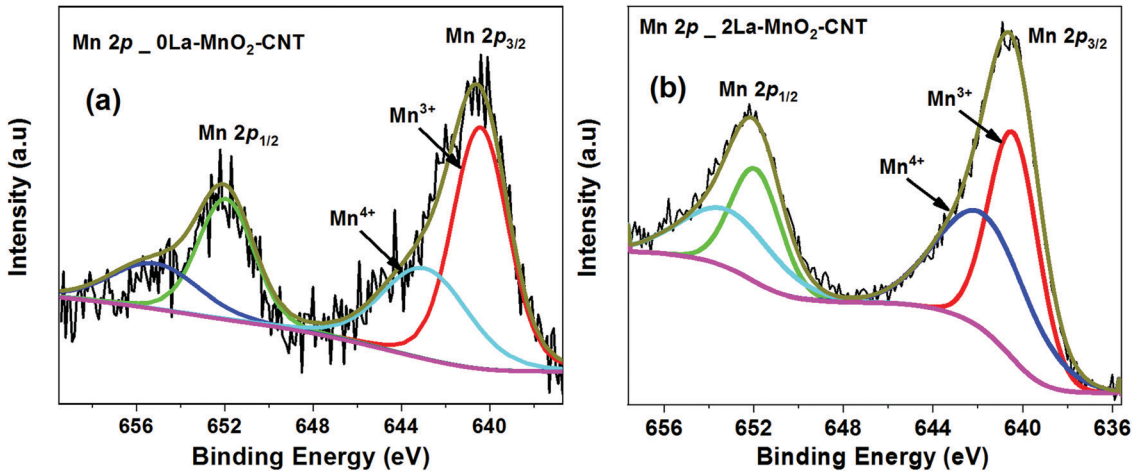

Fig. 3 XPS spectra of Mn 2p of 0La–MnO_2–CNT (a) and 2La–MnO_2–CNT (b).

surface area of the nanohybrid which is highly desirable for electrode application as a larger surface area is likely to facilitate larger ion adsorption.

3.4 Electron microscopic analysis

FESEM image of the 0La–MnO_2–CNT nanohybrid is presented in Fig. 4(a), whereas Fig. 4(b–d) show the elemental mapping data as obtained using EDAX. The FESEM image of the 0La–MnO_2–CNT nanohybrid shows that MnO_2 rod-like structures of diameter 100 nm and 1 μm long are anchored within the CNT network. From elemental mapping, it was further confirmed that the rods are indeed made of Mn and O only, suggesting that the nanorods are made of MnO_2.

Fig. 5(a) represents a typical FESEM image of the 2La–MnO_2–CNT nanohybrid which shows that MnO_2 rod-like structures (diameter 90 nm and 1.2 μm long) are attached to the CNT framework. The elemental mapping data further confirm (Fig. 5(b–e)) the presence of Mn, C, O and La.

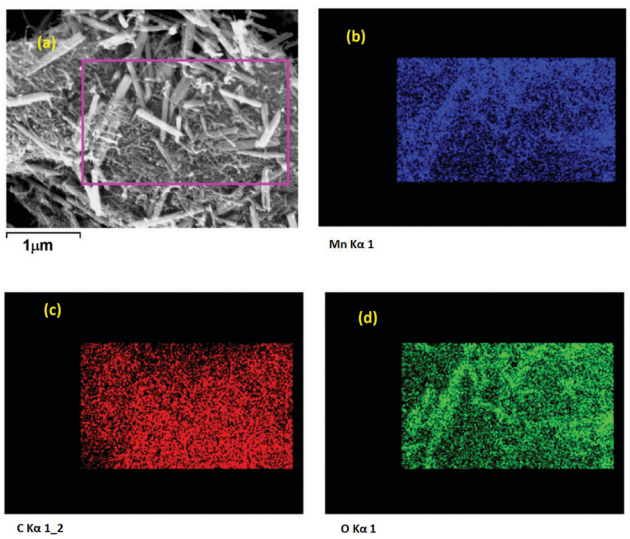

Fig. 4 FESEM (a) and elemental maps of (b) Mn; (c) C, and (d) O for 0La–MnO_2–CNT.

Fig. 6(a) shows an image of a single nanorod of 30 nm diameter of α-MnO_2, whereas Fig. 6(b) shows the high resolution lattice resolved image of α-MnO_2 nanorods showing the presence of (011) planes having a *d* value of 2.40 Angstroms (JCPDS card number 98-001-2177). From the TEM image (Fig. 6(a)) it is clearly observed that the nanorods were bundled together and because of this the average diameter of the nanorods came out to be around 90 nm (Fig. 5(a)). The SAED pattern (Fig. 6(c)) further shows concentric rings corresponding to the (011), (210), (211), (402) and (112) planes of α-MnO_2 nanorods.

3.5 CV analysis

Fig. 7(a) presents the CV curves obtained from 0La–MnO_2–CNT measured at different scan rates (10 mV s^{-1} to 200 mV s^{-1}) under a voltage window of −0.5 to 0.3 V, whereas the inset shows the CV curves at low scan rates (1 mV s^{-1} to 5 mV s^{-1}). The rectangular shape of the CV curves clearly indicates the EDLC behaviour. Along with the presence of a weak pair of redox peaks which confirms the existence of some pseudo-capacitance behaviour along with EDLC. The reduction (or cathodic) peak appears at −0.2 V and the oxidation (or anodic) peak appears at −0.1 V as the result of the reversible redox reaction of Mn^{3+} to Mn^{4+}.[35] Upon charging, MnO_2 is oxidised to MnOOH at the electrode surface while MnOOH is reduced to MnO_2 during discharging. The charge storage mechanism of the nanohybrid is based on the surface adsorption of hydroxyl ions (OH^-) by the electrode material[36] as given below:

$$MnO_2 + OH^- \leftrightarrow MnOOH + H_2O + e^- \quad (1)$$

The CV curves presented in Fig. 7(b–e) were measured using the same measurement parameters for 1, 2, 3 and 5 mol% La^{3+} doped MnO_2–CNT. With the increase in doping concentration of La, the shape of the CV curves becomes more rectangular in shape as compared to that of 0La–MnO_2–CNT which suggests great reversibility in capacitive behaviour for the doped samples. A comparative CV curve at 5 mV s^{-1} of all the nanohybrids is presented in Fig. 7(f). It can be observed that the CV curve of

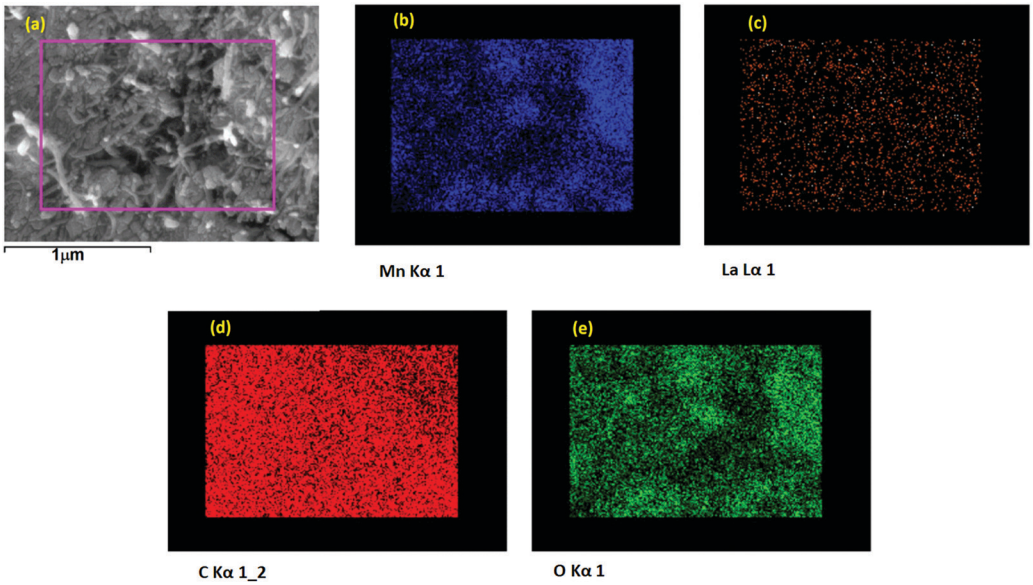

Fig. 5 FESEM (a) and elemental maps of (b) Mn; (c) La; (d) C; and (e) O for 2La–MnO_2–CNT.

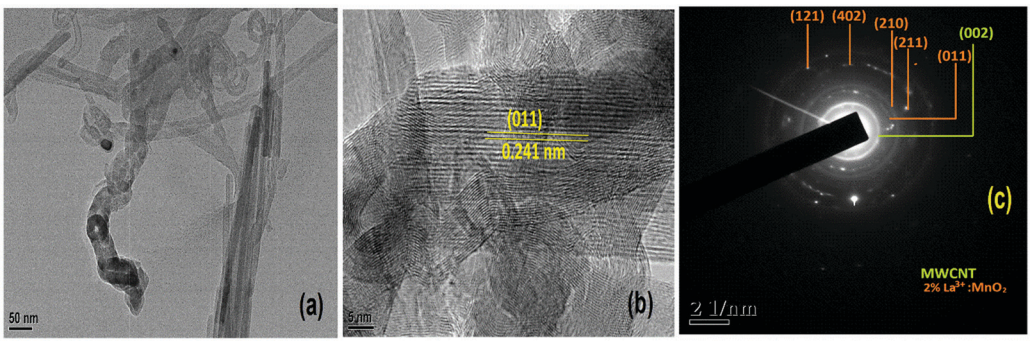

Fig. 6 (a) TEM image; (b) HRTEM image showing a single 2 mol% La^{3+}:MnO_2 attached to CNT; and (c) SAED pattern of 2La–MnO_2–CNT.

2La–MnO_2–CNT has the largest enclosed area and thus is expected to exhibit the highest specific capacitance.

From the CV data (at 5 mV s^{-1}), specific capacitances of 342 F g^{-1}, 707 F g^{-1}, 891 F g^{-1}, 594 F g^{-1} and 245 F g^{-1} for 0La–MnO_2–CNT, 1La–MnO_2–CNT, 2La–MnO_2–CNT, 3La–MnO_2–CNT and 5La–MnO_2–CNT were estimated, respectively. With the increase in doping concentration up to 2 mol% La, the specific capacitance increases and then decreases beyond 2 mol% which can be ascribed to the increase in the electrical conductivity of MnO_2 upon doping up to 2 mol% La. Beyond 2 mol% La doping, there is $La(OH)_3$ formation due to an excess amount of La precursor in the solution mixture during the synthesis process which is in good agreement with the Raman spectra (Fig. 3(a)), XPS studies (Fig. S1 and S2, ESI†) and our previous report on La doping.[26] For doping with low concentration (*i.e.*, 2 mol% La), the mechanism is different as it does not form any additional $La(OH)_3$, rather its role is to create artificial defects within the MnO_2 lattice to enhance its surface area and electrical conductivity which synergistically improves the electrochemical performance. The specific capacitance of all the electrode materials decreases with the increase in scan rate due to reduced diffusion rates of OH^- ions as the interaction time between the electrolyte ions and active electrode material gets too short. Thus, only a small portion of the active electrode material takes part in the redox reaction, as a result of which lower specific capacitance values were obtained at high scan rates.[26,37] However, at low scan rates due to the increase in interaction time, the electrolyte ions get a chance to enter into the pores of the active electrode material due to prolonged exposure. As a result, the redox reaction is more efficient at lower scan rates leading to higher values of specific capacitance.

The charge storage mechanism can be estimated using the power law, $I = av^b$, where the b value determines the charge storage mechanism. The linear plots of $\log(I_{pa})$ *versus* $\log(v)$, generated using (Fig. 8(a)) redox peak currents within the scan range of 1–200 mV s^{-1} for all the samples, confirm that the charge storage is controlled by both capacitive (b = 1) (EDLC) and semi-infinite diffusion mechanism (b = 0.5) (pseudocapacitance) as the 'b'-value for all the nanohybrids lies in between 0.5 and 1.[38–42]

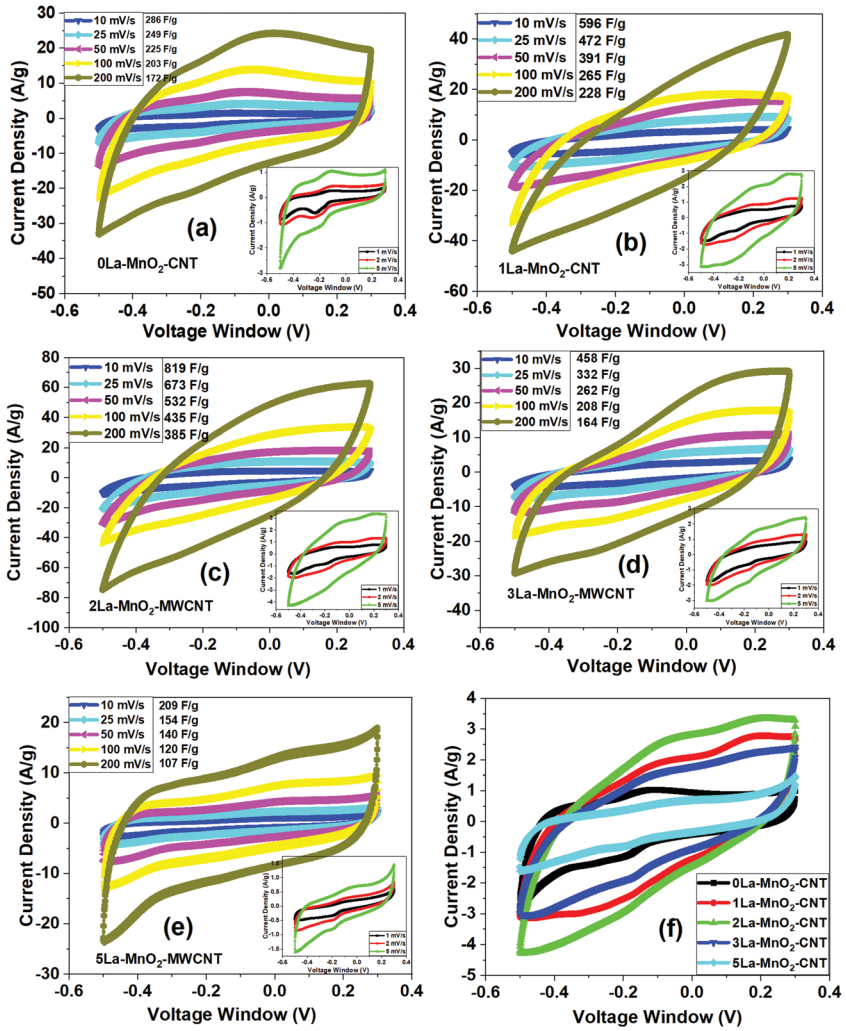

Fig. 7 CV curves of 0La–MnO_2–CNT (a) and various La doped MnO_2–CNT hybrids (b–e) at varying scan rates; (insets of (a–e) show the curves at low scan rates); (f) comparative CV curves of all the samples at 5 mV s^{-1} scan rate.

With the increase in scan rate, the cathodic (I_{pc}) and anodic peak (I_{pa}) current also increases and their ratio (I_{pa}/I_{pc}) was estimated to be ~1 indicating a reversible redox reaction.[43] Both I_{pa} and I_{pc} are not linearly dependant with the square root of scan rates (Fig. 8(b)) but fit well with the power law as shown in the inset of Fig. 8(b), which represents capacitive behaviour. This further confirms that EDLC is dominant over pseudo-capacitance, which is consistent with the shape of the CV curves. A higher diffusion coefficient value of $D = 4.27 \times 10^{-8}$ cm^2 s^{-1} for the 2La–MnO_2–CNT electrode was obtained as compared to that of the 0La–MnO_2–CNT sample ($D = 9.49 \times 10^{-9}$ cm^2 s^{-1}), which can be ascribed to the increase in mobility of electrolyte

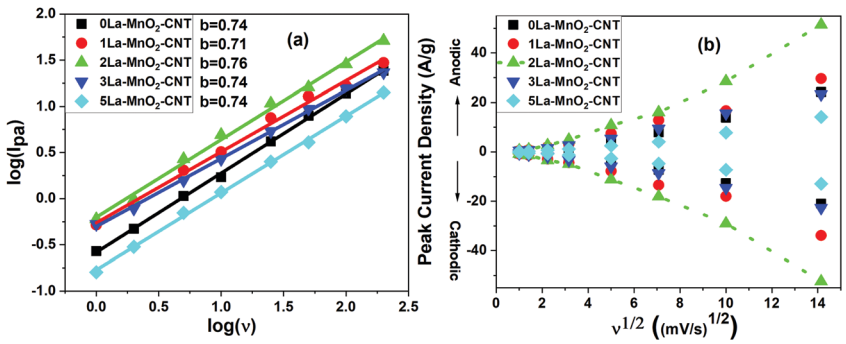

Fig. 8 log of peak current (I_{pc}) *vs.* log(v) plot (a); and I_{pc} *vs.* $v^{1/2}$ plot (b) of all the samples.

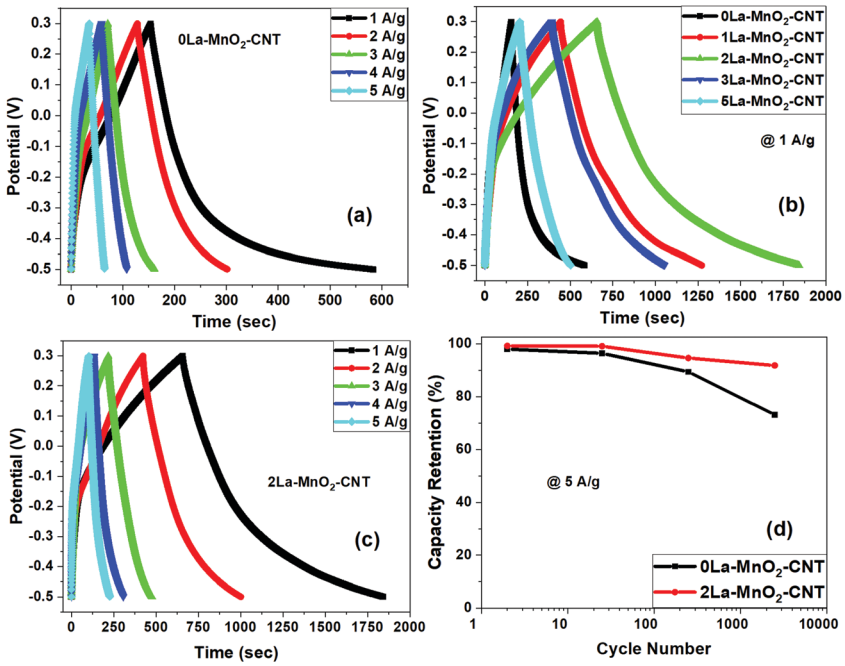

Fig. 9 GCD profiles of 0La–MnO_2–CNT at different constant current densities (a); comparative GCD profiles of undoped and La^{3+} MnO_2–CNT nanohybrids at 1 A g^{-1} (b); GCD profiles of 2La–MnO_2–CNT at 1 A g^{-1} (c); cycle stability of 0La–MnO_2–CNT and 2La–MnO_2–CNT at 5 A g^{-1} up to 5000 cycles (d).

ions into the active electrode material due to the introduction of La^{3+} dopants. Beyond 2 mol% La doping, the diffusion coefficient was found to decrease which might be due to the aggregates of amorphous $La(OH)_3$ hindering the diffusion of electrolyte ions into the pores of the electroactive material.[26,44,45]

3.6 GCD analysis

For 0La–MnO_2–CNT and La doped samples the GCD measurements were carried out at different constant current densities ranging from 1 A g^{-1} to 5 A g^{-1} under the voltage window of −0.5 to 0.3 V, presented in Fig. 9(a). The triangular shape of GCD profiles confirmed the dominance of EDLC behaviour. For the 0La–MnO_2–CNT nanohybrid, the specific capacitance estimated at 1 A g^{-1} was 533 F g^{-1}, which is comparable with that estimated from the CV curve at 1 mV s^{-1} (515 F g^{-1}). The specific capacitance values estimated from the CV curve and GCD profile can only be compared if the applied current density in GCD corresponds to that of the peak current density obtained in the CV curve. Fig. 9(b) presents a comparative GCD profile of all the samples at a constant current density of 1 A g^{-1} which clearly shows that the charging/discharging time increases with the introduction of La^{3+} dopants up to 2 mol%

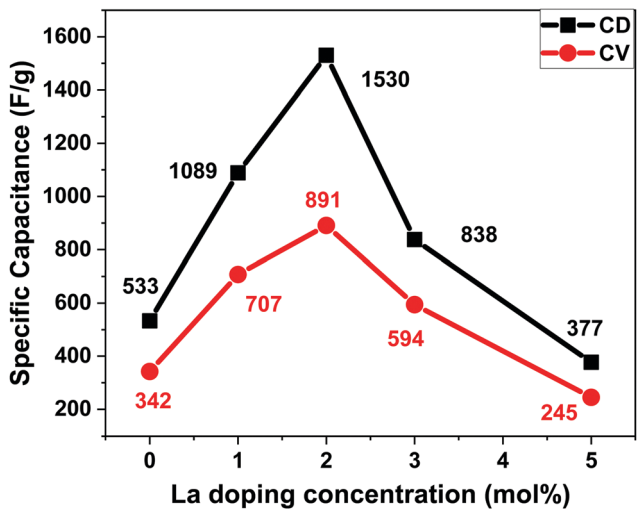

Fig. 10 Specific capacitance *vs.* doping concentration of La from the CV curve at 5 mV s^{-1} and GCD curve at 1 A g^{-1}.

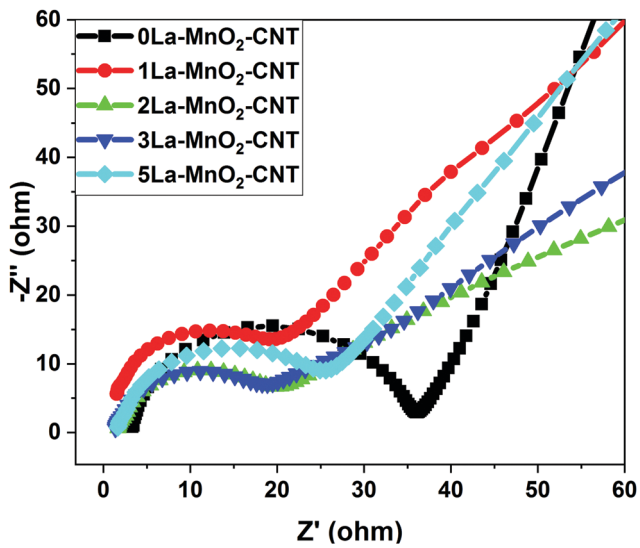

Fig. 11 EIS spectra of undoped and La^{3+}:MnO_2–CNT nanohybrids.

Table 1 ESR and R_{ct} values for undoped and doped nanohybrids as obtained from the Nyquist plots. Also listed are the diffusion coefficients

Electrode material	ESR (Ω)	R_{ct} (Ω)	Diffusion coefficient ($cm^2\ s^{-1}$)
0La–MnO_2–CNT	3.49	33.4	9.49×10^{-9}
1La–MnO_2–CNT	1.81	23.4	3.16×10^{-8}
2La–MnO_2–CNT	1.85	15.8	4.27×10^{-8}
3La–MnO_2–CNT	1.66	16.8	2.33×10^{-8}
5La–MnO_2–CNT	1.49	24.9	9.82×10^{-9}

beyond which it decreases, resulting in lower specific capacitance values for 3% and 5% La doped samples. Specific capacity as high as 1530 F g^{-1} was achieved at 1 A g^{-1} current density for 2La–MnO_2–CNT. Fig. 9(c) plots the GCD profiles of 2La–MnO_2–CNT at different current densities, whereas Fig. 9(d) compares the cycling stability of 0La–MnO_2–CNT and 2La–MnO_2–CNT over 5000 cycles at 5 A g^{-1} which clearly confirmed the superiority of the 2 mol% La doped sample (92% retention) as compared to that of the undoped sample (73%).

For the convenience of the reader, specific capacitance estimated from CV at 5 mV s^{-1} and GCD at 1 A g^{-1} against doping concentration of La are presented in Fig. 10. One can see that both CV and GCD measurements confirm 2 mol% as the optimized concentration of La dopants for the best electrode performance. The large difference in the magnitude of capacitance estimated from the two methods (CV and GCD) is not uncommon in the literature due to the mismatch in current density obtained from the CV curve and applied current density to obtain the charge discharge plot.[19,23,33]

3.7 EIS analysis

From the Nyquist plot presented in Fig. 11, the equivalent series resistance (ESR) and charge transfer resistance (R_{ct}) were estimated from the intercept and diameter of the semi-circle in the Nyquist plot, respectively.[14,26] The small changes in ESR values are due to differences in the conductivities caused by the structural variations from electrode to electrode. However, significant changes in the R_{ct} values were observed for the La-doped samples. The R_{ct} values start decreasing up to 2 mol% La and increase again upon further increase in the doping concentration, which is possibly due to the formation of amorphous $La(OH)_3$ having high electrical resistivity. It could be observed that though the 1 mol% La nanohybrid has slightly higher current density than 3 mol% La, the R_{ct} value of 1 mol% La is higher than that of 3 mol% La, which is possibly due to the occurence of competing processes of defect induced positive effects and negative influence by the formation of amorphous $La(OH)_3$ above 2 mol% La doping. The ESR and R_{ct} values of undoped and La doped MnO_2–CNT hybrids are listed in Table 1, which also lists the diffusion coefficients of the nanohybrids as estimated from CV.

For better understanding of the importance of this work, we have compared the results of this work with those of the previously published reports on MnO_2-based electrodes in Table 2. It is evident that the nanohybrid synthesized in this work shows much better performance in terms of specific capacitance and cycling stability as compared to those of the previous reports. The enhanced performance is due to appropriate choice of material combination and synergistic tailoring of the properties such as surface area and electrical conductivity of the optimised 2La–MnO_2–MWCNT sample.

4. Conclusions

In summary, La^{3+}:MnO_2–CNT nanohybrids were prepared using a simple hydrothermal method for application as a supercapacitor electrode. Several nanohybrids were prepared by varying the concentration of the La precursor, and the influence of dopant concentration on morphology, crystal structure and electrochemical properties was systematically investigated. XRD and electron microscopy revealed the presence of rod-like MnO_2 structures well distributed within the CNT network. The electrochemical studies showed that at 2 mol% La doping, the 2La–MnO_2–CNT nanohybrid exhibited

Table 2 Comparison of the electrochemical performance of La^{3+}:MnO_2–CNT prepared in this work with that of MnO_2 based electrodes reported by other researchers

Material	Brief synthetic procedure	Electrolyte	Specific capacitance	Capacity retention	Ref.
MnO_2/MWCNT	Wet chemical route	1 M Na_2SO_4	201 F g^{-1} at 1 A g^{-1}	~10 000 cycles	17
MnO_2/MWCNT	Wet chemical route	6 M K_2SO_4	Areal capacitance 0.97 F cm^{-2} at 1 A g^{-1}	85% @ 3000 cycles	18
Amorphous MWCNT/MnO_2 nanoflakes	Wet chemical route	1 M Na_2SO_4	145.6 at 5 mV s^{-1} and 108.5 F g^{-1} at 0.7 A g^{-1}	~1400 cycles	19
MnO_2/MWCNT core–shell	Hydrothermal @ 100 °C for 12 h	1 M Na_2SO_4	223 F g^{-1} at 10 mV s^{-1}		20
MnO_2/MWCNT	Wet chemical route	1 M Na_2SO_4	106 F g^{-1} at 0.5 A g^{-1}	95% @ 1000 cycles	21
MnO_2/MWCNT	Electrodeposition	6 M KOH	277 F g^{-1} at 0.5 A g^{-1}	1000 cycles	22
rGO/CNT/MnO_2	Hydrothermal @ 150 °C for 6 h	1 M Na_2SO_4	319 F g^{-1} at 0.5 A g^{-1} 521 F g^{-1} at 5 mV s^{-1}	85% @ 3000 cycles	23
Ag doped MnO_2 on carbon fiber	Electrochemical deposition	0.5 M Na_2SO_4	825 F g^{-1} at 5 mV s^{-1} 815 F g^{-1} at 0.5 A g^{-1}	~3000 cycles	46
Ni doped MnO_2/carbon fiber	Carbonization followed by wet chemical route	1 M Na_2SO_4	445 F g^{-1} at 1 A g^{-1}	93% @ 1000 cycles	47
B doped MnO_2/carbon fiber	Wet chemical route	0.5 M Na_2SO_4	364.8 F g^{-1} at 2 mV s^{-1}	80% @ 1000 cycles	48
2La–MnO_2–CNT nanohybrid	Hydrothermal route	1 M NaOH	891 F g^{-1} at 5 mV s^{-1} 1530 F g^{-1} at 1 A g^{-1}	92% @ 5000 cycles	This work

the best electrode behaviour with a specific capacitance as high as $\sim$1530 F g^{-1} at 1 A g^{-1} current density along with excellent cycling stability (92% retention of specific capacitance after 5000 cycles). The enhanced performance of the optimised 2La–MnO_2–CNT nanohybrid is ascribed to its lowest charge transfer resistance and highest diffusion coefficient compared to those of other samples containing lower or higher dopant concentrations. Thus, the results shown in this report establish the 2La–MnO_2–CNT nanohybrid as a promising candidate for a supercapacitor electrode.

Conflicts of interest

There are no conflicts of interest to declare.

Acknowledgements

The authors acknowledge the MHRD, Govt. of India for funding this research through the ''Centre of Excellence in Advanced Materials'' grant of May 2018 under the Technical Education Quality Improvement Programme (TEQIP) phase III.

References

1 Y. Gogotsi and P. Simon, True Performance Metrics in Electrochemical Energy Storage, *Science*, 2011, **334**, 917–918.
2 P. Simon and Y. Gogotsi, Materials for electrochemical capacitors, *Nat. Mater.*, 2008, **7**, 845.
3 G. Wang, L. Zhang and J. Zhang, A review of electrode materials for electrochemical supercapacitors, *Chem. Soc. Rev.*, 2012, **41**, 797–828.
4 W. Li, J. Xu, Y. Pan, L. An, K. Xu, G. Wang, Z. Yu, L. Yu and J. Hu, A facile synthesis of α-MnO_2 used as a supercapacitor electrode material: The influence of the Mn-based precursor solutions on the electrochemical performance, *Appl. Surf. Sci.*, 2015, **357**, 1747–1752.
5 X. Su, L. Yu, G. Cheng, H. Zhang, M. Sun and X. Zhang, High-performance α-MnO_2 nanowire electrode for supercapacitors, *Appl. Energy*, 2015, **153**, 94–100.
6 S. Zhao, T. Liu, D. Shi, Y. Zhang, W. Zeng, T. Li and B. Miao, Hydrothermal synthesis of urchin-like MnO_2 nanostructures and its electrochemical character for supercapacitor, *Appl. Surf. Sci.*, 2015, **351**, 862–868.
7 X. Zhang, W. Miao, C. Li, X. Sun, K. Wang and Y. Ma, Microwave-assisted rapid synthesis of birnessite-type MnO_2 nanoparticles for high performance supercapacitor applications, *Mater. Res. Bull.*, 2015, **71**, 111–115.
8 H. Xia, C. Hong, X. Shi, B. Li, G. Yuan, Q. Yao and J. Xie, Hierarchical heterostructures of Ag nanoparticles decorated MnO_2 nanowires as promising electrodes for supercapacitors, *J. Mater. Chem. A*, 2015, **3**, 1216–1221.
9 Z. Hu, X. Xiao, L. Huang, C. Chen, T. Li, T. Su, X. Cheng, L. Miao, Y. Zhang and J. Zhou, 2D vanadium doped manganese dioxides nanosheets for pseudocapacitive energy storage, *Nanoscale*, 2015, **7**, 16094–16099.
10 Z. Wang, F. Wang, Y. Li, J. Hu, Y. Lu and M. Xu, Interlinked multiphase Fe-doped MnO_2 nanostructures: A novel design for enhanced pseudocapacitive performance, *Nanoscale*, 2016, **8**, 7309–7317.
11 X. Su, L. Yu, G. Cheng, H. Zhang, M. Sun, L. Zhang and J. Zhang, Controllable hydrothermal synthesis of Cu-doped δ-MnO_2 films with different morphologies for energy storage and conversion using supercapacitors, *Appl. Energy*, 2014, **134**, 439–445.
12 R. Poonguzhali, N. Shanmugam, R. Gobi, A. Senthilkumar, R. Shanmugam and K. Sathishkumar, Influence of Zn doping on the electrochemical capacitor behavior of MnO_2 nanocrystals, *RSC Adv.*, 2015, **5**, 45407–45415.
13 H. Z. Chi, Y. Li, Y. Xin and H. Qin, Boron-doped manganese dioxide for supercapacitors, *Chem. Commun.*, 2014, **50**, 13349–13352.
14 A. Sarkar, A. K. Chakraborty, S. Bera and S. Krishnamurthy, Novel Hydrothermal Synthesis of CoS_2/MWCNT Nanohybrid Electrode for Supercapacitor: A Systematic Investigation on the Influence of MWCNT, *J. Phys. Chem. C*, 2018, **122**, 18237–18246.
15 R. K. Agrawalla, S. Paul, P. K. Sahoo, A. K. Chakraborty and A. K. Mitra, A facile synthesis of a novel three-phase nanocomposite: single-wall carbon nanotube/silver nanohybrid fibers embedded in sulfonated polyaniline, *J. Appl. Polym. Sci.*, 2015, **132**, 41692.
16 A. K. Chakraborty and K. S. Coleman, Poly(ethylene) glycol/single-walled carbon nanotube composites, *J. Nanosci. Nanotechnol.*, 2008, **8**, 4013–4016.
17 L. Li, Z. A. Hu, N. An, Y. Y. Yang, Z. M. Li and H. Y. Wu, Facile Synthesis of MnO_2/CNTs Nanohybrid for Supercapacitor Electrodes with Long Cycle Stability, *J. Phys. Chem. C*, 2014, **118**, 22865–22872.
18 K. Wang, S. Gao, Z. Du, A. Yuan, W. Lu and L. Chen, MnO_2-Carbon nanotube nanohybrid for high-areal-density supercapacitors with high rate performance, *J. Power Sources*, 2016, **305**, 30–36.
19 D. Ganguly, D. Pahari, N. S. Das, P. Howli, B. Das, D. Banerjee and K. K. Chattopadhyay, All-amorphous CNT-MnO_2 nanoflaky hybrid for improved supercapacitor applications, *J. Electroanal. Chem.*, 2016, **778**, 12–22.
20 H. Xia, Y. Wang, J. Lin and L. Lu, Hydrothermal synthesis of MnO_2/CNT nanonanohybrid with a CNT core/porous MnO_2 sheath hierarchy architecture for supercapacitors, *Nanoscale Res. Lett.*, 2012, **7**, 33.
21 D. Z. W. Tan, H. Cheng, S. T. Nguyen and H. M. Duong, Controlled synthesis of MnO_2/CNT nanonanohybrids for supercapacitor applications, *Mater. Technol.*, 2014, **29**, A107–A113.
22 S. Liu, Y. Liu, W. Song, J. Song, C. Wang, G. Shao and X. Qin, Flocky MnO_2/carbon nanotube nanohybrids electrodeposited under supergravity field for supercapacitors, *J. Solid State Electrochem.*, 2015, **19**, 1321–1329.
23 H. Jiang, Y. Dai, Y. Hu, W. Chen and C. Li, Nanostructured ternary nanonanohybrid of rGO/CNTs/MnO_2 for high-rate supercapacitors, ACS Sustain, *Chem. Eng.*, 2014, **2**, 70–74.

24 S. M. D. Watson, K. S. Coleman, A. K. Chakraborty and A. New, Route to the Production and Nanoscale Patterning of Highly Smooth, Ultrathin Zirconium Oxide Films, *ACS Nano*, 2008, **2**, 643–650.

25 S. P. Mondal, A. Dhar, S. K. Ray and A. K. Chakraborty, Bonding, vibrational, and electrical characteristics of CdS nanostructures embedded in polyvinyl alcohol matrix, *J. Appl. Phys.*, 2009, **105**, 084309.

26 N. Chakrabarty and A. K. Chakraborty, Controlling the electrochemical performance of β-$Ni(OH)_2$/carbon nanotube hybrid electrodes for supercapacitor applications by La doping: A systematic investigation, *Electrochim. Acta*, 2019, **297**, 173–187.

27 S. R. Sanivarapu, J. B. Lawrence and G. Sreedhar, Role of Surface Oxygen Vacancies and Lanthanide Contraction Phenomenon of $Ln(OH)_3$ (Ln = La, Pr, and Nd) in Sulfide-Mediated Photoelectrochemical Water Splitting, *ACS Omega*, 2018, **3**, 6267–6278.

28 D. Wang, K. Wang, L. Sun, H. Wu, J. Wang, Y. Zhao, L. Yan, Y. Luo, K. Jiang, Q. Li, S. Fan, J. Li and J. Wang, MnO_2 nanoparticles anchored on carbon nanotubes with hybrid supercapacitor-battery behavior for ultrafast lithium storage, *Carbon*, 2018, **139**, 145–155.

29 T.-H. Kim, M.-H. Park, J. Ryu and C.-W. Yang, Oxidation Mechanism of Nickel Oxide/Carbon Nanotube Nanohybrid, *Microsc. Microanal.*, 2013, **19**, 202–206.

30 Y.-S. Li, J.-L. Liao, S.-Y. Wang and W.-H. Chiang, Intercalation-assisted longitudinal unzipping of carbon nanotubes for green and scalable synthesis of graphene nanoribbons, *Sci. Rep.*, 2016, **6**, 22755.

31 H. Liu, Z. Hu, L. Tian, Y. Su, H. Ruan, L. Zhang and R. Hu, Reduced graphene oxide anchored with δ-MnO_2 nanoscrolls as anode materials for enhanced Li-ion storage, *Ceram. Int.*, 2016, **42**, 13519–13524.

32 R. R. Salunkhe, H. Ahn, J. H. Kim and Y. Yamauchi, Rational design of coaxial structured carbon nanotube–manganese oxide (CNT–MnO_2) for energy storage application, *Nanotechnology*, 2015, **26**, 204004.

33 H. Xia, M. Lai and L. Lu, Nanoflaky MnO_2/carbon nanotube nanohybrids as anode materials for lithium-ion batteries, *J. Mater. Chem.*, 2010, **20**, 6896–6902.

34 Y. Jeon, D. H. Park, J. Il Park, S. H. Yoon, I. Mochida, J. H. Choy and Y. G. Shul, Hollow fibers networked with perovskite nanoparticles for H2 production from heavy oil, *Sci. Rep.*, 2013, **3**, 1–8.

35 M. Liu, L. Gan, W. Xiong, Z. Xu, D. Zhu and L. Chen, Development of MnO_2/porous carbon microspheres with a partially graphitic structure for high performance supercapacitor electrodes, *J. Mater. Chem. A*, 2014, **2**, 2555–2562.

36 L. Li, Z. Du, S. Liu, Q. Hao, Y. Wang, Q. Li and T. Wang, A novel nonenzymatic hydrogen peroxide sensor based on MnO_2/graphene oxide nanonanohybrid, *Talanta*, 2010, **82**, 1637–1641.

37 N. Chakrabarty, A. K. Chakraborty and H. Kumar, Nickel Hydroxide Nanohexagon Based High Performance Electrode for Supercapacitor: A Systematic Investigation on the Influence of Six Different Carbon Nanostructures, *J. Phys. Chem. C*, 2019, **123**, 29104–29115.

38 M. Sathiya, A. S. Prakash, K. Ramesha, J. Tarascon and A. K. Shukla, V2O5-Anchored Carbon Nanotubes for Enhanced Electrochemical Energy Storage, *J. Am. Chem. Soc.*, 2011, **133**, 16291–16299.

39 J. Duay, S. A. Sherrill, Z. Gui, E. Gillette and S. B. Lee, Self-LimitingElectrodeposition of Hierarchical MnO_2 and M(OH)2/MnO_2 Nanofibril/Nanowires: Mechanism and Supercapacitor Properties, *ACS Nano*, 2013, **7**, 1200–1214.

40 H. Yin, C. Song, Y. Wang, S. Li, M. Zeng, Z. Zhang, Z. Zhu and K. Yu, Influence of morphologies and pseudocapacitive contributions for charge storage in V2O5 micro/nanostructures, *Electrochim. Acta*, 2013, **111**, 762–770.

41 M. Zhu, W. Meng, Y. Huang, Y. Huang and C. Zhi, Proton-Insertion-EnhancedPseudocapacitance Based on the Assembly Structure of Tungsten Oxide, *ACS Appl. Mater. Interfaces*, 2014, **6**, 18901–18910.

42 N. Chakrabarty, A. Dey, S. Krishnamurthy and A. K. Chakraborty, CeO_2/Ce_2O_3 quantum dot decoratedreduced graphene oxide nanohybrid as electrode for supercapacitor, *Appl. Surf. Sci.*, 2021, **536**, 147960.

43 I. Chakraborty, N. Chakrabarty, A. Senapati and A. K. Chakraborty, CuO@NiO/Polyaniline/MWCNT nanonanohybrid as high-performance electrode for supercapacitor, *J. Phys. Chem. C*, 2018, **122**, 27180–27190.

44 A. Muthusamy and A. Paul, Importance of Electrode Preparation Methodologies in Supercapacitor Applications, *ACS Omega*, 2017, **2**, 8039–8050.

45 S. Zhang, H. Sha, R. H. R. Castro and R. Faller, Atomistic modeling of La^{3+} doping segregation effect on nanocrystallineyttria-stabilized zirconia, *Phys. Chem. Chem. Phys.*, 2018, **20**, 13215–13223.

46 Z. Zeng, P. Sun, J. Zhu and X. Zhu, Ag-doped manganese oxide prepared by electrochemical deposition on carbon fiber for supercapacitors, *RSC Adv.*, 2015, **5**, 17550–17558.

47 J. Li, Y. Ren, S. Wang, Z. Ren and J. Yu, Transition metal doped MnO_2 nanosheets grown on internal surface of macroporous carbon for supercapacitors and oxygen reduction reaction electrocatalysts, Appl, *Mater. Today*, 2016, **3**, 63–72.

48 H. Z. Chi, H. Zhu and L. Gao, Boron-doped MnO_2/carbon fiber nanohybrid electrode for supercapacitor, *J. Alloys Compd.*, 2015, **645**, 199–205.